Journal of Materials Chemistry A

ROYAL SOCIETY OF CHEMISTRY

PAPER

View Article Online
View Journal | View Issue

Cite this: J. Mater. Chem. A, 2020, 8, 24743

Ultrafine oxygen-defective iridium oxide nanoclusters for efficient and durable water oxidation at high current densities in acidic media†

Zhipeng Yu,‡[ab] Junyuan Xu,‡[a] Yifan Li,‡[c] Bin Wei,[a] Nan Zhang,[a] Yue Li,[ad] Oleksandr Bondarchuk,[a] Hongwei Miao,[a] Ana Araujo,[a] Zhongchang Wang,[a] Joaquim Luis Faria,[b] Yuanyue Liu*[c] and Lifeng Liu*[a]

Received 20th July 2020
Accepted 2nd November 2020

DOI: 10.1039/d0ta07093a

rsc.li/materials-a

Iridium oxide (IrO_2) is one of the best known electrocatalysts for the oxygen evolution reaction (OER) taking place in a strongly acidic solution. IrO_2 nanocatalysts with high activity as well as long-term catalytic stability, particularly at high current densities, are highly desirable for proton exchange membrane water electrolysis (PEM-WE). Here, we report a simple and cost-effective strategy for depositing ultrafine oxygen-defective IrO_x nanoclusters (1–2 nm) on a high-surface-area, acid-stable titanium current collector (H-Ti@IrO_x), through a repeated impregnation–annealing process. The high catalytically active surface area resulting from the small size of IrO_x and the preferable electronic structure originating from the presence of oxygen defects enable the outstanding OER performance of H-Ti@IrO_x, with low overpotentials of 277 and 336 mV to deliver 10 and 200 mA cm^{-2} in 0.5 M H_2SO_4. Moreover, H-Ti@IrO_x also shows an intrinsic specific activity of 0.04 mA $cm_{catalyst}^{-2}$ and superior mass activity of 1500 A g_{Ir}^{-1} at an overpotential of 350 mV. Comprehensive experimental studies and density functional theory calculations confirm the important role of oxygen defects in the enhanced OER performance. Remarkably, H-Ti@IrO_x can continuously catalyze the OER in 0.5 M H_2SO_4 at 200 mA cm^{-2} for 130 hours with minimal degradation, and with a higher IrO_x loading, it can sustain at such a high current density for over 500 hours without significant performance decay, holding substantial promise for use in PEM-WE.

Introduction

Developing electrochemical energy conversion devices, such as fuel cells and water electrolyzers, is of paramount importance to the future energy sustainability and environmental remediation.[1] Electrocatalytic water splitting has recently regained considerable research interest as a sustainable and carbon-neutral approach to the production of hydrogen (H_2) – a promising energy carrier that has the potential to replace conventional fossil fuels.[2–4] In particular, proton exchange membrane water electrolysis (PEM-WE) has shown significant advantages over the conventional alkaline water electrolysis (AWE) technology, because PEM-WE allows for higher energy efficiency, production of purer H_2 gas, compact system design, and dynamic flexibility of operation.[5–7] However, the development of PEM electrolyzers is largely hindered by the lack of highly active and stable electrocatalysts to efficiently catalyze the oxygen evolution reaction (OER) in acidic solutions.[8] Up to now, iridium (Ir)-based materials are the best known OER electrocatalysts with both high activity and reasonably good stability in acidic media.[8–13] However, large-scale deployment of PEM electrolyzers is restricted by the low earth abundance and high cost of iridium.[10,14–16]

To enable widespread deployment of PEM water electrolyzers, the OER catalytic performance of Ir-based catalysts must be drastically improved and meanwhile the Ir utilization should be kept as minimal as possible. To this end, much research effort has been dedicated to nanostructuring Ir and doping Ir with non-precious transition metals, aiming to enhance the intrinsic catalytic activity and to better utilize the precious Ir.[17] For example, nanoclusters of IrO_x–Ir and IrRu alloy,[18,19] bimetallic IrNi,[20] nanoporous[21] and ultra-small IrO_2 (ref. 22) have been reported to show good OER performance in acid media, with a low overpotential to deliver the benchmark current

[a]International Iberian Nanotechnology Laboratory (INL), Av. Mestre Jose Veiga, 4715-330 Braga, Portugal. E-mail: lifeng.liu@inl.int

[b]Laboratory of Separation and Reaction Engineering-Laboratory of Catalysis and Materials (LSRE-LCM), Faculdade de Engenharia, Universidade do Porto, Rua Dr. Roberto Frias s/n 4200-465 Porto, Portugal

[c]Texas Materials Institute, Department of Mechanical Engineering, University of Texas at Austin, USA. E-mail: yuanyue.liu@austin.utexas.edu

[d]Center of Chemistry, Chemistry Department, University of Minho, Gualtar Campus, Braga, 4710-057, Portugal

† Electronic supplementary information (ESI) available. See DOI: 10.1039/d0ta07093a

‡ These authors contributed equally to this work.

density of 10 mA cm^{-2}.[18–22] In addition, a number of studies have shown that structural defects have a significant impact on the electronic structure and surface properties of catalysts, and intentional or accidental introduction of defects into catalysts may enhance their catalytic activity, which has been verified in a few nonprecious metal based catalysts.[23,24] Recent studies have also demonstrated that non-stoichiometric and defective oxygen in the lattice of iridium oxide or ruthenium oxide may markedly boost the intrinsic activity of these catalysts for the OER.[25–29] This makes defect engineering a useful strategy to enhance the catalytic activity.

While various strategies have been developed to improve the activity of Ir-based catalysts, achieving long-term stability in strongly acidic media, particularly at a high current density, remains a great challenge. The harsh, corrosive and oxidative environment may give rise to dissolution and/or over-oxidation of catalytically active species, leading to the rapid loss of OER catalytic activity.[30–32] For these reasons, most Ir-based OER catalysts reported so far can only survive at a low current density (typically $\leq$10 mA cm^{-2}) for a limited period of time (a few to tens of hours),[14,15,25–29] which is far from what is required for practical industry-relevant PEM-WE.

Herein, we develop iridium oxide (IrO_x) nanoclusters combining the advantages of an ultrafine cluster size (1–2 nm), which leads to the exposure of a large active surface area, and an oxygen-defective feature, which results in an electronic structure favorable for the OER. By loading IrO_x nanoclusters on hydrothermally treated high-surface-area titanium foam (H-Ti foam), outstanding OER catalytic activity has been achieved in a strongly acidic solution (*i.e.*, 0.5 M H_2SO_4), with low overpotentials (η) of 277 and 336 mV to deliver current densities of 10 and 200 mA cm^{-2}, respectively. Moreover, the intimate contact between IrO_x and H-Ti foam significantly stabilizes the IrO_x nanocluster catalysts. As a result, the H-Ti foam supported IrO_x (H-Ti@IrO_x) is able to continuously catalyze the OER at a high current density of 200 mA cm^{-2} in 0.5 M H_2SO_4 for 130 hours without notable degradation. Moreover, density functional theory (DFT) calculations confirm that the oxygen defects in IrO_x result in a low binding energy of oxygenated intermediates, especially of the oxygen atoms, leading to a markedly decreased energy barrier to the catalytic reaction and thus higher OER performance in the IrO_x.

Results and discussion

The H-Ti@IrO_x catalyst was prepared by soaking H-Ti foam in 0.1 M aqueous solution of $IrCl_3$ for 30 min, followed by thermal annealing at 400 °C in air for 30 min. The IrO_x loading density can be adjusted by repeating the impregnation–annealing cycles. Using a similar process, IrO_x was also loaded on pristine Ti foam (P-Ti@IrO_x) and a carbon paper substrate (C@IrO_x) for use as controls.

Hydrothermal treatment of Ti foam in high-concentration KOH solution (10 M) led to the formation of a high density of cross-linked nanowires (NWs, 20–30 nm in diameter) on the foam surface (Fig. S1, ESI†), which may significantly increase the number of sites that can immobilize IrO_x nanoclusters. The same morphology was observed as well on hydrothermally treated Ti foam in a recent report.[33] According to the X-ray diffractometry (XRD) examination results, only a very weak diffraction peak from $KHTi_4O_9 \cdot 0.5H_2O$ (PHT, ICDD no. 00-038-0173) was detected for H-Ti (Fig. S1a, ESI†), besides those from metallic Ti (ICDD no. 04-015-0276). This indicates that the formed PHT NWs have poor crystallinity. Furthermore, the formation of $KHTi_4O_9 \cdot 0.5H_2O$ was confirmed by Raman spectroscopy (Fig. 1a), where the Raman peaks at 200, 280, 440, and 650 cm^{-1} can be well assigned to the Ti-OH vibration in $KHTi_4O_9 \cdot 0.5H_2O$.[34,35]

Fig. 1b shows the XRD patterns of the as-prepared H-Ti@IrO_x catalyst and the control samples of C@IrO_x and P-Ti@IrO_x. No diffraction peaks from IrO_2 can be resolved for H-Ti@IrO_x and P-Ti@IrO_x, suggesting that the deposited iridium oxide may either be poorly crystallized or consist of tiny crystallites that significantly widen the diffraction peaks.

The morphology and microstructure of H-Ti@IrO_x catalysts were further examined by scanning electron microscopy (SEM) and transmission electron microscopy (TEM). Loading IrO_x nanoclusters on H-Ti foam did not markedly alter its morphology, as revealed by SEM examination (Fig. S2, ESI†). Fig. 1c shows a representative low-magnification TEM image of PHT NWs loaded with IrO_x catalysts, where a high density of nanoclusters are found to distribute on the surface of NWs (representative nanoclusters marked with yellow circles). These nanoclusters have a typical size of 1–2 nm and are crystallized, as shown in the high resolution TEM (HRTEM) image in Fig. 1d. The measured lattice fringe of 0.258 nm corresponds to the (101) crystal planes of tetragonal IrO_2 (ICDD no. 00-015-0870). The crystal structure of nanoclusters was further examined in the high-angle annular dark field scanning transmission electron microscopy (HAADF-STEM) mode, where a dense distribution of nanoclusters on the NW surface can be distinguished more clearly (Fig. 1e and f). The atomic-resolution HAADF-STEM imaging (Fig. 1g) confirmed that the lattice of nanoclusters matches well the atomic model of tetragonal IrO_2 with defective oxygen, viewed along the [100] direction (Fig. 1h), which can be further corroborated by the fast Fourier transformation electron diffraction (FFT-ED) analyses (Fig. 1g, inset). Furthermore, STEM elemental mapping (Fig. 1i) illustrated that Ir covers on the PHT NWs with a very high density.

We also examined the crystal structure and morphology of H-Ti@IrO_x with different IrO_x loading densities. No XRD peaks from any polymorph of iridium oxides were detected even if the loading density was increased to 0.6 mg cm^{-2} (Fig. S3, ESI†). Moreover, the morphology did not change as the loading density varied (Fig. S4, ESI†). Furthermore, we investigated the microstructure of IrO_x clusters deposited on the P-Ti foam and carbon paper substrate. In P-Ti@IrO_x, IrO_x exhibits the same tetragonal crystal structure, but has a bigger cluster size and broader size distribution (4–10 nm, Fig. S5, ESI†); while for C@IrO_x, the deposited IrO_x is interconnected forming a porous structure where the size of ligaments falls in the range of 2–3 nm (Fig. S6, ESI†), similar to the morphology of cluster beam deposited Ru clusters we reported previously.[36] This suggests that both the size and uniformity of the deposited IrO_x

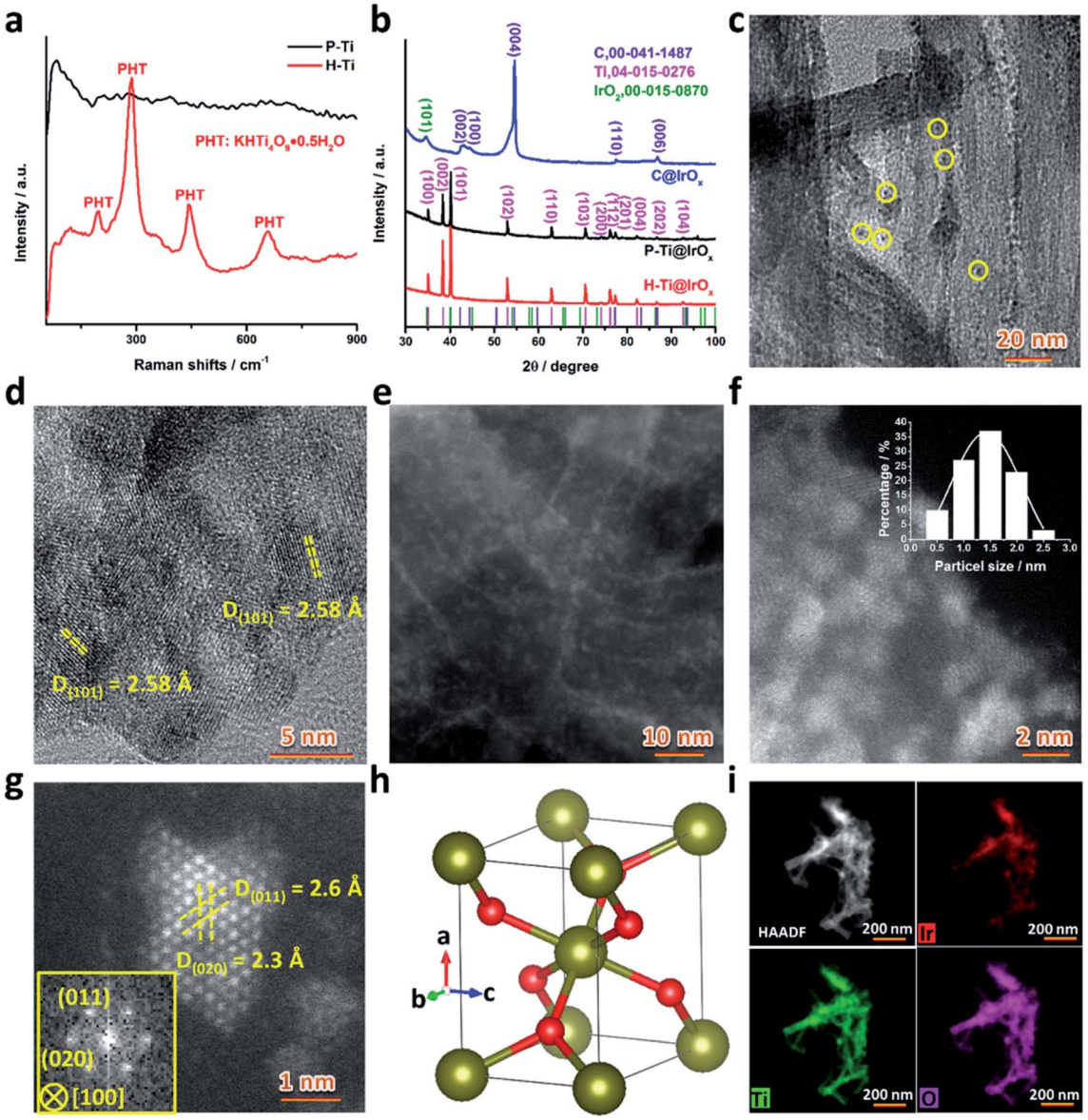

Fig. 1 (a) Raman spectra of H-Ti foam and P-Ti foam. (b) XRD patterns of H-Ti@IrO_x, P-Ti@IrO_x, and C@IrO_x. (c) Bright-field TEM image and (d) HRTEM image of H-Ti@IrO_x. (e) Low-magnification and (f) high-magnification HAADF-STEM image of IrO_x catalysts. (g) Atomic-resolution STEM image of an individual IrO_x nanocluster. Inset: the corresponding FFT-ED pattern. (h) Schematic illustration of the crystal structure in (g). Yellow and red spheres represent Ir and O atoms, respectively. (i) HAADF-STEM image and the corresponding elemental maps of Ir, Ti and O.

nanoclusters are influenced by the catalyst support. When the H-Ti foam was immersed in $IrCl_3$ solution, Ir^{3+} cations tended to bond with the hydroxyl groups on the surface of PHT NWs *via* electrostatic interaction.[34] The subsequent thermal annealing in air oxidized the chemisorbed iridium and immobilized the formed IrO_x nanoclusters on the H-Ti foam. Simultaneous nucleation at multiple sites resulted in the formation of size-uniform ultrafine nanoclusters. A similar nucleation process also happened on the oxidized carbon paper, where a large quantity of hydroxyl functional groups exist on the surface,[37,38] leading to the formation of small IrO_x clusters. In contrast, the pristine P-Ti foam does not have as many oxyl or hydroxyl groups on its surface as the H-Ti foam or carbon paper, and therefore, the IrO_x deposited on the P-Ti foam is larger in size and shows a wider size distribution.

We have investigated the surface chemical states of H-Ti@IrO_x, P-Ti@IrO_x, C@IrO_x, and commercial IrO_2 particles using X-ray photoelectron spectroscopy (XPS). The XPS survey spectra confirm the presence of corresponding elements in each catalyst (Fig. S7, ESI†). Given that XPS allows the investigation of the local chemical (ionic) environment of materials,[39] it has been used to characterize the degree of oxygen deficiency and related valence state change of metal cations in metal oxides.[23,24] Fig. 2 shows the O 1s XPS spectra of H-Ti@IrO_x and other control catalysts, which can be de-convoluted into four components. The binding energy (BE) peak at *ca.* 529.8 eV (O1)

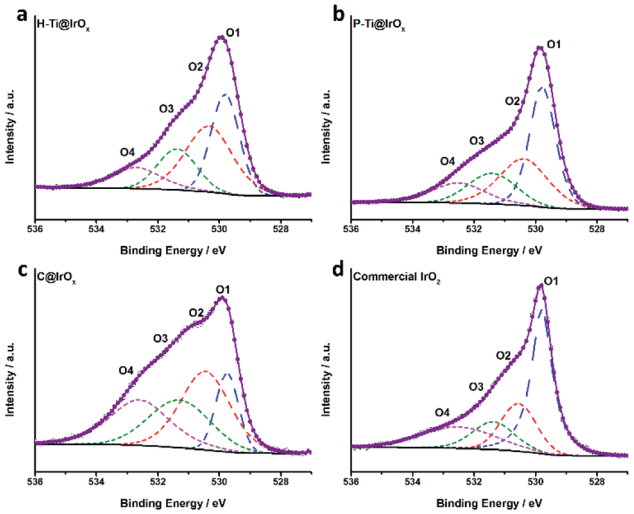

Fig. 2 O 1s spectra of (a) H-Ti@IrO$_x$, (b) P-Ti@IrO$_x$, (c) C@IrO$_x$, and (d) commercial IrO$_2$ particles.

generally relates to metal–oxygen bonding, the BE peak at 531.4 eV (O3) can be assigned to surface –OH groups, and the BE peak at 532.6 eV (O4) is associated with water.[40] In the literature, the BE peak centered around 530.4 eV (O2) has been proposed to correlate with surface oxygen defects, reflecting the degree of oxygen deficiency (*i.e.*, the stoichiometry of oxygen with metal cations).[24,25] XPS quantitative analysis manifests that the content of the surface defective oxygen is 37.0%, 34.4%, 28.5%, and 20.5% in H-Ti@IrO$_x$, C@IrO$_x$, P-Ti@IrO$_x$, and commercial IrO$_2$ particles, respectively (Table S1, ESI†), indicating that the Ir/O stoichiometry in H-Ti@IrO$_x$ deviates heavily from 1 : 2 and the IrO$_x$ nanoclusters in H-Ti@IrO$_x$ are severely oxygen-defective. The high-resolution Ir 4f XPS spectra of all the catalysts are compared in Fig. S8 (ESI).† There exist two spin–orbit components in the spectra, corresponding to the Ir 4f$_{5/2}$ and Ir 4f$_{7/2}$ components, respectively, which can be further deconvoluted into nine components characteristic of Ir^{IV}, Ir^{III}, Ir^{IV} satellite 1, Ir^{IV} satellite 2 and Ir^{III} satellite, respectively (Fig. S8, Tables S2 and S3, ESI†).[41,42] Notably, we found that the ratio of Ir^{III}/Ir^{IV} increases as the content of surface defective oxygen increases, following the order H-Ti@IrO$_x$ > C@IrO$_x$ > P-Ti@IrO$_x$ > commercial IrO$_2$, in consistence with the degree of oxygen deficiency in these catalysts, which indicates that the Ir^{III} valence state correlates with the O2 component in O 1s spectra. The Ir^{III} valence state likely results from the transfer of electrons trapped at the oxygen-defective sites to Ir^{IV} cations.[41,42]

The OER activity of H-Ti@IrO$_x$ with different IrO$_x$ loading densities was first assessed at room temperature in 0.5 M H_2SO_4 (pH = 0.3), and H-Ti@IrO$_x$ loaded with 0.25 mg cm^{-2} IrO$_x$ was found to outperform all others under the same testing conditions in terms of not only the apparent catalytic activity but also the Ir-mass based activity and the intrinsic specific activity obtained through normalizing the catalytic current with the electrocatalytically active surface area, *i.e.*, ECSA (Fig. S9–11, ESI†). Therefore, the H-Ti@IrO$_x$-0.25 mg cm^{-2} sample (denoted as H-Ti@IrO$_x$ for simplicity hereafter) was used in further investigation and comparison with other control catalysts.

Fig. 3a shows the polarization curves of H-Ti@IrO$_x$ and control catalysts including P-Ti@IrO$_x$, C@IrO$_x$, and commercial IrO$_2$, which were recorded in 0.5 M H_2SO_4 at a scan rate of 5 mV s^{-1}. The H-Ti foam subjected to thermal annealing treatment the same as that for preparing H-Ti@IrO$_x$ does not show appreciable anodic current density (Fig. S12, ESI†). Upon loading IrO$_x$, the OER catalytic current density of H-Ti@IrO$_x$ is significantly enhanced. The H-Ti@IrO$_x$ can deliver geometric current densities of 10, 100, and 200 mA cm$_{geo}^{-2}$ at low overpotentials (η) of 277, 318 and 336 mV, respectively (Fig. 3a), remarkably lower than those of P-Ti@IrO$_x$ (η_{10} = 343 mV), C@IrO$_x$ (η_{10} = 328 mV), and commercial IrO$_2$ (η_{10} = 556 mV), even if the loading densities of iridium oxide are similar to or lower than these control catalysts (0.39 mg cm^{-2} for P-Ti@IrO$_x$, 0.24 mg cm^{-2} for C@IrO$_x$, and 0.39 mg cm^{-2} for commercial IrO$_2$ particles).

To assess the intrinsic catalytic performance, the ECSA-normalized specific activities of H-Ti@IrO$_x$ and other control catalysts, which reflect the reactivity of each active site, were calculated and compared. The ECSA was obtained by cyclic voltammetry measurements in the non-faradaic potential region (see Experimental details), and it shows the following

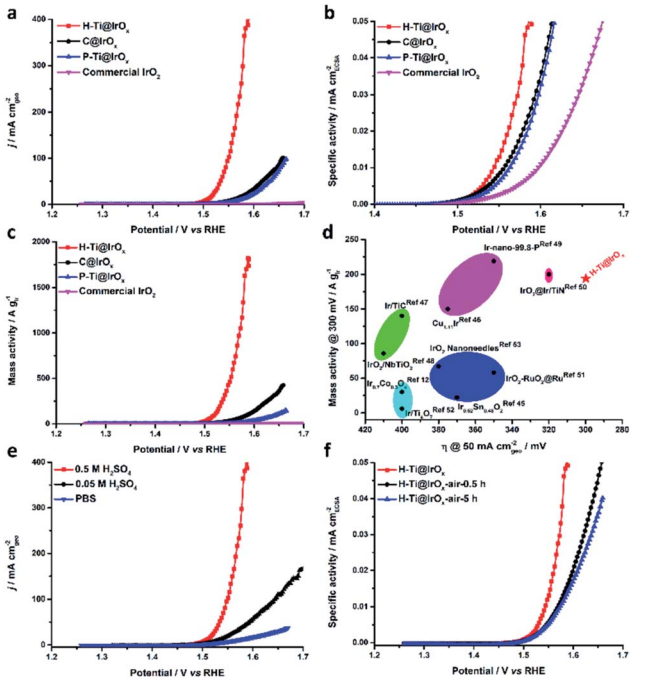

Fig. 3 OER performance of H-Ti@IrO$_x$ and other control catalysts. (a) *iR*-corrected polarization curves of H-Ti@IrO$_x$, C@IrO$_x$, P-Ti@IrO$_x$ and commercial IrO$_2$ catalysts, recorded at a scan rate of 5 mV s^{-1} in 0.5 M H_2SO_4. (b) Specific activities and (c) mass activities of H-Ti@IrO$_x$, C@IrO$_x$, P-Ti@IrO$_x$ and commercial IrO$_2$ catalysts in 0.5 M H_2SO_4. (d) Comparison of the OER performance of H-Ti@IrO$_x$ catalysts to that of other state-of-the-art OER catalysts. (e) *iR*-corrected polarization curves of H-Ti@IrO$_x$ catalysts, recorded at a scan rate of 5 mV s^{-1} in electrolytes with different pH values. (f) Specific activities of H-Ti@IrO$_x$, H-Ti@IrO$_x$-air-0.5 h and H-Ti@IrO$_x$-air-5 h in 0.5 M H_2SO_4.

order: H-Ti@IrO_x (7086 $cm_{catalyst}^{-2}$) > C@IrO_x (828 $cm_{catalyst}^{-2}$) > P-Ti@IrO_x (357 $cm_{catalyst}^{-2}$) > commercial IrO_2 (37 $cm_{catalyst}^{-2}$), as revealed in Fig. S13 (ESI†). The exceptionally high ECSA of H-Ti@IrO_x may result, on the one hand, from the ultra-small size feature of IrO_x nanoclusters and ultra-high specific surface area of the PHT NW support, and on the other hand, likely from the high number of oxygen defects in H-Ti@IrO_x.[23] Despite the exceptionally high surface area, after normalization the H-Ti@IrO_x catalyst still exhibits a higher specific activity, able to deliver 0.04 mA $cm_{catalyst}^{-2}$ at $\eta = 350$ mV (Fig. 3b), 2.4, 2.0 and 6.5 times more active than P-Ti@IrO_x, C@IrO_x, and commercial IrO_2, respectively.

The mass activities of all catalysts, an important consideration for practical applications, were also calculated and are compared in Fig. 3c. The H-Ti@IrO_x catalyst outperforms all control catalysts, capable of delivering a mass activity as high as 1500 A g_{Ir}^{-1} at $\eta = 350$ mV, which is 20, 89 and 2041 higher than that of C@IrO_x, P-Ti@IrO_x and commercial IrO_2, respectively. The mass activity of H-Ti@IrO_x is also higher than that of commercial Ir-based catalysts from different industrial suppliers.[43] To better reflect the utilization of precious Ir, the mass activity of H-Ti@IrO_x at $\eta = 300$ mV is further plotted against the apparent catalytic activity η_{50} and compared to that of previously reported state-of-the-art Ir-based catalysts, as shown in Fig. 3d. An optimal catalyst should show both high apparent activity (*i.e.*, low overpotential at a given current density) and high mass activity, namely, utilization of the minimum possible precious metal(s) without sacrificing the apparent catalytic current density (positioned in the upper right region in Fig. 3d).[14,44] In this respect, our H-Ti@IrO_x catalyst indeed outperforms many other Ir-based OER catalysts,[12,45–53] indicating that the Ir in H-Ti@IrO_x is optimally utilized.

The reaction kinetics of all catalysts was studied by Tafel analysis. As shown in Fig. S14a (ESI†), the H-Ti@IrO_x catalyst exhibits a small Tafel slope of 29 mV dec^{-1}, which is markedly smaller than that of C@IrO_x (60 mV dec^{-1}), P-Ti@IrO_x (60 mV dec^{-1}) and commercial IrO_2 (85 mV dec^{-1}), indicating more favorable OER kinetics. The electrochemical impedance spectroscopy (EIS) measurements also confirmed the fast reaction rate of H-Ti@IrO_x for the OER, as evidenced by its much smaller charge transfer resistance (R_{ct}) than that of other control catalysts (Fig. S14b, ESI†). It is hypothesized that the oxygen defects might give rise to reactive oxygen species such as O^{I-} reported by Schlögl and co-workers,[41,42,54] the electrophilic nature of which would help accelerate the formation of the OOH intermediates, leading to fast OER kinetics.[54]

Given the corrosive nature of strong acids, it is preferable to perform PEM-WE in weak acids or environmentally more friendly neutral media. However, developing OER electrocatalysts active in weak acids and neutral solutions remains a great challenge.[2] We have tested the OER performance of H-Ti@IrO_x in 0.05 M H_2SO_4 and phosphate buffered saline (PBS) solution (pH = 7.2), respectively. Interestingly, H-Ti@IrO_x likewise exhibits very good OER activity in these electrolytes (Fig. 3e). For instance, it only needs an overpotential of 414 mV to generate a high catalytic current density of 100 mA cm^{-2} in 0.05 M H_2SO_4. Furthermore, in PBS electrolyte it can deliver 10 mA cm^{-2} at a low overpotential of 339 mV, showing substantial promise for use in PEM-WE in neutral solutions.

We hypothesize that the content of oxygen-defective sites in the H-Ti@IrO_x catalysts may play an important role in their outstanding OER performance. To validate this hypothesis, we managed to anneal H-Ti@IrO_x in air for 0.5 and 5 h (denoted as H-Ti@IrO_x-air-0.5 h and H-Ti@IrO_x-air-5 h, respectively). XPS analyses proved that the content of oxygen-defective sites was decreased to 32.6% and 27.0% for H-Ti@IrO_x-air-0.5 h and H-Ti@IrO_x-air-5 h, respectively, from the initial 37.0%, and meanwhile, the ratio of Ir^{III}/Ir^{IV} in the catalysts decreased accordingly (Fig. S15, Tables S1 and S2, ESI†). Moreover, the ECSA of thermally annealed H-Ti@IrO_x was remarkably reduced as well (Fig. S16a–c, ESI†). Accordingly, the apparent catalytic activities of H-Ti@IrO_x-air-0.5 h and H-Ti@IrO_x-air-5 h become poorer, and larger overpotentials of 372 and 381 mV are needed to afford 100 mA cm^{-2} for H-Ti@IrO_x-air-0.5 h and H-Ti@IrO_x-air-5 h, respectively (Fig. S16d, ESI†). Furthermore, the specific activity of H-Ti@IrO_x becomes deteriorated upon thermal annealing (Fig. 3f), which suggests that the intrinsic catalytic performance of H-Ti@IrO_x is indeed closely related to the content of oxygen-defective sites in IrO_x.

Density functional theory (DFT) calculations were performed to gain further insight into the role of oxygen defects in promoting the OER performance. The (110) facet of the tetragonal (rutile-phase) IrO_2 without (perfect IrO_2, denoted as p-IrO_2) and with oxygen defects (*i.e.*, IrO_x) was used as a model surface, in accordance with the previous reports.[55–57] Fig. 4a shows the reaction steps during the OER with the related oxygenated intermediates of OH*, O*, OOH* and OO*, based on the conventional adsorbate evolution mechanism (AEM). To study how the number of oxygen defects influences the catalytic performance, IrO_x models with a single oxygen-defective site at five possible sites (denoted as mono-IrO_x, Fig. S17, ESI†) and with double oxygen-defective sites at seven possible sites (denoted as bi-IrO_x, Fig. S18, ESI†) were developed and the thermodynamically most stable models were identified (Fig. S17 and S18, ESI†). The OER Gibbs free energy diagrams of p-IrO_2, mono-IrO_x, and bi-IrO_x were calculated at a potential of $U = 1.50$ V based on the optimized models (Fig. 4b–d). For p-IrO_2 and mono-IrO_x, the calculations reveal that the last elementary reaction step ($OO^* \rightarrow O_2\uparrow + *$) is the rate determining step (RDS), and the energy barrier (2.23 eV) is significantly higher for the Ir site in p-IrO_2 (labelled with a light blue circle in Fig. 4b, inset) than that (1.21 eV) for the Ir site in mono-IrO_x (labelled with a light blue circle in Fig. 4c, inset). This indicates that introducing an oxygen-defective site into IrO_x indeed decreases the energy barrier in the RDS and enhances the OER activity. Interestingly, for bi-IrO_x the RDS has been altered to the second elementary step ($OH^* \rightarrow O^* + H^+ + e^-$) with a much lower energy barrier of 0.51 eV, suggesting that the OER activity is further improved as the number of oxygen defects increases. The Gibbs energy calculations agree well with the experimental observation where the intrinsic OER activity increases with the increasing content of oxygen defects (Fig. 3b and f). It is worth noting that the same trend is also valid for the Gibbs free energy diagrams calculated at $U = 1.23$ V (Fig. S19, ESI†).

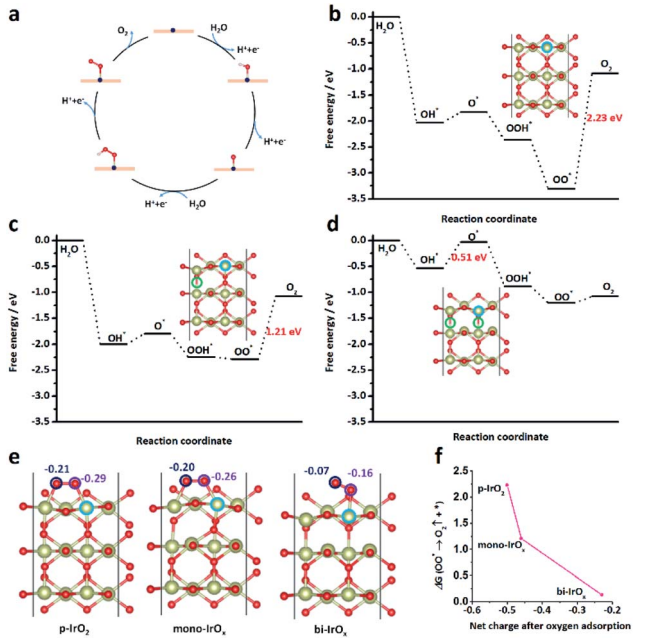

Fig. 4 (a) The proposed 4e$^-$ OER mechanism in the present work. Calculated Gibbs free-energy diagrams for the OER on (b) p-IrO_2, (c) mono-IrO_x and (d) bi-IrO_x at $U = 1.50$ V. The inset shows the corresponding calculation model of each catalyst. The catalyst models of mono-IrO_x and bi-IrO_x are the optimized ones. (e) Net charge analysis of oxygen atoms adsorbed on p-IrO_2 (left), mono-IrO_x (middle) and bi-IrO_x (right). (f) The net charge relative to the Gibbs energy barrier of the oxygen desorption step in p-IrO_2, mono-IrO_x and bi-IrO_x. The yellow and red spheres represent Ir and O atoms, respectively, in all models. The active site, oxygen-defective site and adsorbed oxygen atoms are labelled with light blue, green, violet and navy circles in the each model used for calculation.

To further scrutinize the oxygen defect induced enhancement in OER performance, the optimal adsorption structures of all reaction intermediates were identified and the binding energy of the reaction intermediates to the model catalysts was calculated. As shown in Fig. S20a (ESI),† all the reaction intermediates bind strongly to the p-IrO_2 surface, which causes high energy barriers for the OER.[55] Incorporation of an oxygen-defective site (*i.e.*, mono-IrO_x) weakens the binding of all intermediates to IrO_x, especially that of the adsorbed oxygen atoms (Fig. S20b, ESI†), thus decreasing the energy barrier of the RDS (OO* $\rightarrow$ $O_2\uparrow$ + *). Incorporating one more oxygen-defective site further reduces the binding energy of OO*, and the oxygen desorption step is not the RDS any more in bi-IrO_x; moreover, the energy barrier of the RDS in bi-IrO_x markedly diminishes due to the optimized adsorption of all reaction intermediates (Fig. S20c, ESI†). All these results suggest that the enhanced OER performance could be largely attributed to the decreased binding energy of reaction intermediates to the catalyst as the oxygen defects are introduced.

Furthermore, the net charge induced by the adsorbed oxygen atoms at the Ir site was calculated and compared (Fig. 4e). The net charge is -0.46 e in mono-IrO_x, lower than that of -0.50 e in p-IrO_2, which implies that the oxygen adsorption is weakened around the Ir site, and accordingly, the energy barrier of the RDS is reduced and the OER performance is promoted (Fig. 4f). The net charge further decreases to -0.23 e in bi-IrO_x, and in this case, the oxygen molecule release step (OO* $\rightarrow$ $O_2\uparrow$ + *) shows an even lower energy barrier (Fig. 4f). Meanwhile, the partial density of states (PDOS) calculations reveal markedly reduced overlay of the Ir d-orbital and O p-orbital in defect-rich catalysts (Fig. S21, ESI†), corroborating the decreased adsorption of oxygen atoms in mono-IrO_x and bi-IrO_x.

While the above calculations are made based on the conventional adsorbate evolution mechanism, it was recently reported that the lattice oxygen may also participate in the OER generating oxygen through the lattice oxygen mechanism (LOM), especially in hydrous IrO_x.[10,58,59] To assess to which degree the LOM would contribute to the OER, we calculated the Gibbs free energy of reaction intermediates on p-IrO_2, mono-IrO_x, and bi-IrO_x based on the LOM at $U = 1.50$ V (see Experimental details, ESI†).[60] As shown by the free energy diagrams (Fig. S22, ESI†), the energy barrier to overcome for the O* + O_{lat} $\rightarrow$ $O_2\uparrow$ + V_o step (RDS) for all model catalysts *via* the LOM, where O_{lat} and V_o represent the lattice oxygen and the oxygen vacancy (defect), respectively, is much higher than that of the RDS of the catalysts *via* the AEM (Fig. 4b–d), suggesting that the desorption of the evolved oxygen from the catalyst lattice would be difficult and the OER on our IrO_x catalysts is unlikely to occur *via* the LOM. Our calculations are consistent with the recent theoretical research on the AEM and LOM of IrO_2, where oxygen-defective IrO_2 is demonstrated to be less LOM active than RuO_2.[60] In fact, even for the previously reported electrodeposited hydrous IrO_x where the LOM works toward the OER, the contribution of oxygen evolution from the lattice oxygen is fairly small, compared to the oxygen evolved through the AEM.[58]

Overall, our DFT calculations are in good agreement with the experimental data of OER tests (Fig. 3), highlighting the prominent role of oxygen defects in the improvement of OER catalytic performance by weakening the binding of all intermediates to IrO_x. This is also consistent with previous studies on IrO_x,[41,42] in which "O holes" are proposed to contribute to higher catalytic activity.

Stability is a critically important indicator of electrocatalysts for practical applications in water electrolyzers, especially in a strongly acidic environment. Many catalysts are subjected to fast dissolution and/or loss of active phases under corrosive and highly oxidative conditions, leading to poor stability of only a few hours.[14,15,25–30,57,61] We have examined the catalytic stability of H-Ti@IrO_x and other control catalysts in 0.5 M H_2SO_4 using chronopotentiometry (CP) at a large current density of 200 mA cm^{-2} relevant to practical applications. As illustrated in Fig. 5a, C@IrO_x shows a gradual degradation initially and a sharp increase in potential when the OER is going on for only about 1.5 h (Fig. 5a, inset). The failure might result from the significant corrosion of the carbon paper during the OER at a high current density, which led to the detachment of IrO_x nanoclusters from the carbon microfiber surface. This was confirmed by our energy-dispersive X-ray (EDX) spectroscopy, where it showed that *ca.* 82% of the initial Ir loading is lost after the stability test in only a short period of time (*i.e.*, 1.5 h, Fig. S23, ESI†). The Ir loss can be suppressed in case IrO_x is

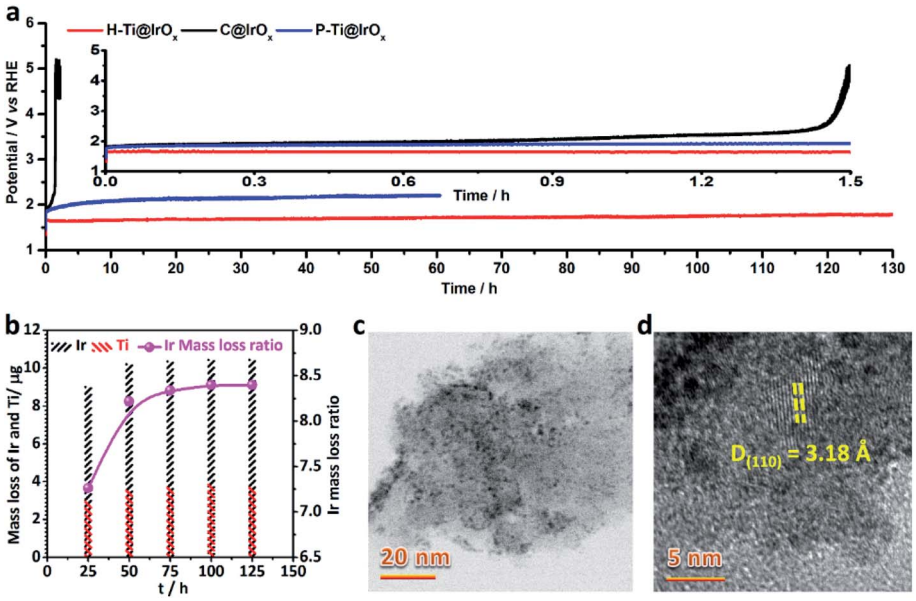

Fig. 5 (a) Chronopotentiometric curves of H-Ti@IrO$_x$ and other control catalysts, recorded at a constant current density of 200 mA cm^{-2} in 0.5 M H_2SO_4. The inset shows the zoomed in view of the initial 1.5 h. (b) ICP analysis of the dissolution of Ir and Ti in H-Ti@IrO$_x$ during the OER electrolysis at 200 mA cm^{-2} after different time intervals. (c) Low-magnification TEM image and (d) HRTEM image of H-Ti@IrO$_x$ after the extended stability test at 200 mA cm^{-2} for 130 h.

loaded on a corrosion-resistant, acid-stable support such as Ti foam, as verified by the stability test of P-Ti@IrO$_x$ catalysts at 200 mA cm^{-2} for 60 h, where only 55% of the initial Ir got lost in 60 h (Fig. S24, ESI†). Compared to C@IrO$_x$ and P-Ti@IrO$_x$, the H-Ti@IrO$_x$ catalyst exhibited superior stability and was able to sustain at 200 mA cm^{-2} for continuous OER electrolysis of 130 h with minimal degradation. According to EDX analysis, merely 22% of the initial Ir is lost in this case (Fig. S25, ESI†). Meanwhile, the Ir dissolution in the electrolyte was monitored using inductively coupled plasma-optical emission spectroscopy (ICP-OES) (Fig. 5b), where we found an Ir loss of only 8.4% after the stability test. The discrepancy in EDX and ICP results can be explained by the fact that some physically detached yet undissolved IrO$_x$ nanoclusters cannot be detected by ICP.[30] We further examined the microstructure of H-Ti@IrO$_x$ after the extended stability test at 200 mA cm^{-2}. Remarkably, a high density of uniformly distributed IrO$_x$ nanoclusters with sizes of 1–2 nm still remained on the surface of PHT NWs and remained crystalline (Fig. 5c and d). Furthermore, using XPS we investigated the chemical states of the H-Ti@IrO$_x$ catalyst subjected to the extended stability test, and we found that both Ir 4f and O 1s spectra (Fig. S26, ESI†) show features pretty similar to those of freshly prepared H-Ti@IrO$_x$ (Fig. 2a and S8a, ESI†). All the above analyses verify that the corrosion-resistant H-Ti support (as proved by the trace amounts of Ti dissolution observed by ICP, Fig. 5b) indeed substantially stabilizes IrO$_x$ and significantly suppresses its loss under harsh conditions, thereby giving rise to excellent catalytic stability. Moreover, the stability number as a metric for electrocatalyst stability benchmarking is also calculated,[59,62] and our H-Ti@IrO$_x$ catalysts show a stability number of 4.27 × 10^6, which is much higher than that of IrO$_x$ nanoparticles (5–6.5 × 10^4),[59] $SrCo_{0.9}Ir_{0.1}O_{3-\delta}$ (8 × 10^4),[62] Ba_2PrIrO_6 (0.7–2.5 × 10^4),[63] and comparable to that of crystalline IrO_2 (0.7–3 × 10^6).[59] In fact, with a higher IrO$_x$ loading density (*e.g.*, H-Ti@IrO$_x$-0.60 mg cm^{-2}), the H-Ti@IrO$_x$ can survive for a significantly longer period of time (above 500 h) at 200 mA cm^{-2} (Fig. S27, ESI†), even though the catalytic activity is compromised a bit. In addition, the faradaic efficiency of O_2 evolution by H-Ti@IrO$_x$ was measured (Fig. S28, ESI†). The volume of O_2 detected matches well with that calculated, indicating a nearly 100% faradaic efficiency in the process of the OER.

Conclusions

In summary, we have deposited ultrafine oxygen-defective iridium oxide nanoclusters on a hydrothermally treated, high-surface-area, acid-stable porous titanium current collector, using a repetitive impregnation–annealing process. Benefiting from the large electrocatalytically accessible surface area and intrinsically high activity arising from the oxygen defects, the obtained H-Ti@IrO$_x$ electrode exhibits excellent apparent, specific, and mass activities for the OER in both acidic and neutral electrolytes, outperforming most of the Ir-based OER catalysts reported before. Comprehensive experimental and theoretical studies confirm that oxygen defects play an important role in the enhanced OER performance. More importantly, we demonstrate that the H-Ti@IrO$_x$ electrode can sustain continuous acidic OER electrolysis at a high current density of 200 mA cm^{-2} for 130 hours without notable degradation, and increasing IrO$_x$ loading to a certain level allows the electrode to catalyze the OER at such a high current density over 500 hours with little performance decay. Given the simplicity of the fabrication procedures and the high mass activity and excellent

long-term stability, the porous titanium foam loaded with ultrafine oxygen-defective iridium oxide nanoclusters holds substantial promise for use as a high-performance anode in proton exchange membrane water electrolyzers.

Author contributions

Z. P. Yu and J. Y. Xu conceived the experiments and drafted the first version of the manuscript. Z. P. Yu synthesized the catalysts and performed XRD, SEM and electrocatalytic tests. J. Y. Xu performed the ICP-OES test. Y. F. Li and Y. Y. Liu performed DFT calculations. B. Wei, H. W. Miao and Z. C. Wang carried out the TEM characterization and did microstructural analyses. Z. P. Yu, Y. Li, O. Bondarchuk and N. Zhang contributed to XPS measurements and analysis. J. L. Faria and A. Araujo contributed to the discussion. L. Liu wrote the final version of the manuscript and coordinated the project.

Conflicts of interest

There are no conflicts to declare.

Acknowledgements

Z. P. Yu acknowledges the financial supported offered by the China Scholarship Council (Grant no. 201806150015). This work was partially funded by the European Regional Development Fund (ERDF) through the COMPETE2020 programme and by the FCT through the MicrophotOGen (POCI-01-0145-FEDER-030674) and TACIT (02/SAICT/2017/028837) projects as well as by the National Innovation Agency of Portugal through the Mobilizador Programme (Baterias 2030, POCI-01-0247-FEDER-046109). Y. Liu acknowledges the support by the Welch Foundation (Grant no. F-1959-20180324) and the National Science Foundation (Grant no. 1900039 and no. 2029442), and the computational resources provided by the National Renewable Energy Lab, the Extreme Science and Engineering Discovery Environment (XSEDE) through allocation TG-CHE190065, the Center for Nanoscale Materials at Argonne National Lab, and the Center for Nanophase Materials Sciences at the Oak Ridge National Lab.

Notes and references

1 G. M. Wang, Y. Yang, D. D. Han and Y. Li, *Nano Today*, 2017, **13**, 23–39.
2 N. T. Suen, S. F. Hung, Q. Quan, N. Zhang, Y. J. Xu and H. M. Chen, *Chem. Soc. Rev.*, 2017, **46**, 337–365.
3 W. Li, D. H. Xiong, X. F. Gao and L. F. Liu, *Chem. Commun.*, 2019, **55**, 8744–8763.
4 X. W. Li, X. G. Hao, A. Abudula and G. Q. Guan, *J. Mater. Chem. A*, 2016, **4**, 11973–12000.
5 M. Carmo, D. L. Fritz, J. Mergel and D. Stolten, *Int. J. Hydrogen Energy*, 2013, **38**, 4901–4934.
6 J. Y. Xu, D. Aili, Q. F. Li, E. Christensen, J. O. Jensen, W. Zhang, M. K. Hansen, G. Y. Liu, X. D. Wang and N. J. Bjerrum, *Energy Environ. Sci.*, 2014, **7**, 820–830.
7 M. Bernt and H. A. Gasteiger, *J. Electrochem. Soc.*, 2016, **163**, F3179–F3189.
8 T. Reier, M. Oezaslan and P. Strasser, *ACS Catal.*, 2012, **2**, 1765–1772.
9 J. Y. Xu, M. Wang, G. Y. Liu, J. L. Li and X. D. Wang, *Electrochim. Acta*, 2011, **56**, 10223–10230.
10 A. Grimaud, A. Demortière, M. Saubanère, W. Dachraoui, M. Duchamp, M. L. Doublet and J. M. Tarascon, *Nat. Energy*, 2016, **2**, 16189.
11 D. F. Abbott, D. Lebedev, K. Waltar, M. Povia, M. Nachtegaal, E. Fabbri, C. Copéret and T. J. Schmidt, *Chem. Mater.*, 2016, **28**, 6591–6604.
12 W. Hu, H. W. Zhong, W. Liang and S. L. Chen, *ACS Appl. Mater. Interfaces*, 2014, **6**, 12729–12736.
13 E. Oakton, D. Lebedev, M. Povia, D. F. Abbott, E. Fabbri, A. Fedorov, M. Nachtegaal, C. Copéret and T. J. Schmidt, *ACS Catal.*, 2017, **7**, 2346–2352.
14 L. C. Seitz, C. F. Dickens, K. Nishio, Y. Hikita, J. Montoya, A. Doyle, C. Kirk, A. Vojvodic, H. Y. Hwang, J. K. Norskov and T. F. Jaramillo, *Science*, 2016, **353**, 1011–1014.
15 L. Yang, G. T. Yu, X. Ai, W. S. Yan, H. L. Duan, W. Chen, X. T. Li, T. Wang, C. H. Zhang, X. R. Huang, J. S. Chen and X. X. Zou, *Nat. Commun.*, 2018, **9**, 5236.
16 C. V. Pham, M. Bühler, J. Knöppel, M. Bierling, D. Seeberger, D. Escalera-López, K. J. J. Mayrhofer, S. Cherevko and S. Thiele, *Appl. Catal., B*, 2020, **269**, 118762.
17 C. Wang, F. L. Lan, Z. F. He, X. F. Xie, Y. H. Zhao, H. Hou, L. Guo, V. Murugadoss, H. Liu, Q. Shao, Q. Gao, T. Ding, R. B. Wei and Z. H. Guo, *ChemSusChem*, 2019, **12**, 1576–1590.
18 P. Lettenmeier, L. Wang, U. Golla-Schindler, P. Gazdzicki, N. A. Cañas, M. Handl, R. Hiesgen, S. S. Hosseiny, A. S. Gago and K. A. Friedrich, *Angew. Chem., Int. Ed.*, 2016, **55**, 742–746.
19 J. Y. Xu, Z. Lian, B. Wei, Y. Li, O. Bondarchuk, N. Zhang, Z. P. Yu, A. Araujo, I. Amorim, Z. C. Wang, B. Li and L. F. Liu, *ACS Catal.*, 2020, **10**, 3571–3579.
20 T. Reier, Z. Pawolek, S. Cherevko, M. Bruns, T. Jones, D. Teschner, S. Selve, A. Bergmann, H. N. Nong, R. Schlögl, K. J. J. Mayrhofer and P. Strasser, *J. Am. Chem. Soc.*, 2015, **137**, 13031–13040.
21 Q. Li, J. J. Li, J. Y. Xu, N. Zhang, Y. P. Li, L. F. Liu, D. Pan, Z. C. Wang and F. L. Deepak, *ACS Appl. Energy Mater.*, 2020, **3**, 3736–3744.
22 J. Q. Guan, D. Li, R. Si, S. Miao, F. X. Zhang and C. Li, *ACS Catal.*, 2017, **7**, 5983–5986.
23 D. F. Yan, Y. X. Li, J. Huo, R. Chen, L. M. Dai and S. Y. Wang, *Adv. Mater.*, 2017, **29**, 1606459.
24 T. Zhang, M. Y. Wu, D. Y. Yan, J. Mao, H. Liu, W. B. Hu, X. W. Du, T. Ling and S. Z. Qiao, *Nano Energy*, 2018, **43**, 103–109.
25 R. X. Ge, L. Li, J. W. Su, Y. C. Lin, Z. Q. Tian and L. Chen, *Adv. Energy Mater.*, 2019, **9**, 1901313.
26 Y. C. Pi, J. Guo, Q. Shao and X. Q. Huang, *Chem. Mater.*, 2018, **30**, 8571–8578.
27 B. M. Tackett, W. C. Sheng, S. Kattel, S. Y. Yao, B. H. Yan, K. A. Kuttiyiel, Q. Y. Wu and J. G. Chen, *ACS Catal.*, 2018, **8**, 2615–2621.

28 J. W. Su, R. X. Ge, K. M. Jiang, Y. Dong, F. Hao, Z. Q. Tian, G. X. Chen and L. Chen, *Adv. Mater.*, 2018, **30**, 1801351.
29 Q. Feng, Q. Wang, Z. Zhang, Y. Y. H. Xiong, H. Y. Li, Y. Yao, X. Z. Yuan, M. C. Williams, M. Gu, H. Chen, H. Li and H. J. Wang, *Appl. Catal., B*, 2019, **244**, 494–501.
30 H. S. Oh, H. N. Nong, T. Reier, A. Bergmann, M. Gliech, J. Ferreira de Araújo, E. Willinger, R. Schlögl, D. Teschner and P. Strasser, *J. Am. Chem. Soc.*, 2016, **138**, 12552–12563.
31 C. Spöri, J. T. H. Kwan, A. Bonakdarpour, D. P. Wilkinson and P. Strasser, *Angew. Chem., Int. Ed.*, 2017, **56**, 5994–6021.
32 S. Cherevko, T. Reier, A. R. Zeradjanin, Z. Pawolek, P. Strasser and K. J. J. Mayrhofer, *Electrochem. Commun.*, 2014, **48**, 81–85.
33 L. L. Zhao, Q. Cao, A. L. Wang, J. Z. Duan, W. J. Zhou, Y. H. Sang and H. Liu, *Nano Energy*, 2018, **45**, 118–126.
34 T. Kokubo and S. Yamaguchi, *Materials*, 2010, **3**, 48–63.
35 C. Caparrós, M. Ortiz-Hernandez, M. Molmeneu, M. Punset, J. A. Calero, C. Aparicio, M. Fernández-Fairén, R. Perez and F. J. Gil, *J. Mater. Sci.: Mater. Med.*, 2016, **27**, 151.
36 J. Y. Xu, S. Murphy, D. H. Xiong, R. S. Cai, X. K. Wei, M. Heggen, E. Barborini, S. Vinati, R. E. Dunin-Borkowski, R. E. Palmer and L. F. Liu, *ACS Appl. Energy Mater.*, 2018, **1**, 3013–3018.
37 J. Y. Xu, T. F. Liu, J. J. Li, B. Li, Y. F. Liu, B. S. Zhang, D. H. Xiong, I. Amorim, W. Li and L. F. Liu, *Energy Environ. Sci.*, 2018, **11**, 1819–1827.
38 J. Y. Xu, J. J. Li, D. H. Xiong, B. S. Zhang, Y. F. Liu, K. H. Wu, I. Amorim, W. Li and L. F. Liu, *Chem. Sci.*, 2018, **9**, 3470–3476.
39 A. Sarkar and G. G. Khan, *Nanoscale*, 2019, **11**, 3414–3444.
40 R. Kötz, H. Neff and S. Stucki, *J. Electrochem. Soc.*, 1984, **131**, 72–77.
41 V. Pfeifer, T. E. Jones, J. J. Velasco Vélez, C. Massué, M. T. Greiner, R. Arrigo, D. Teschner, F. Girgsdies, M. Scherzer, J. Allan, M. Hashagen, G. Weinberg, S. Piccinin, M. Hävecker, A. Knop-Gericke and R. Schlögl, *Phys. Chem. Chem. Phys.*, 2016, **18**, 2292–2296.
42 V. Pfeifer, T. E. Jones, J. J. Velasco Vélez, C. Massué, R. Arrigo, D. Teschner, F. Girgsdies, M. Scherzer, M. T. Greiner, J. Allan, M. Hashagen, G. Weinberg, S. Piccinin, M. Hävecker, A. Knop-Gericke and R. Schlögl, *Surf. Interface Anal.*, 2016, **48**, 261–273.
43 S. M. Alia, B. Rasimick, C. Ngo, K. C. Neyerlin, S. S. Kocha, S. Pylypenko, H. Xu and B. S. Pivovar, *J. Electrochem. Soc.*, 2016, **163**, F3105–F3112.
44 H. N. Nong, T. Reier, H. S. Oh, M. Gliech, P. Paciok, T. H. T. Vu, D. Teschner, M. Heggen, V. Petkov, R. Schlögl, T. Jones and P. Strasser, *Nat. Catal.*, 2018, **1**, 841–851.
45 G. F. Li, H. M. Yu, X. Y. Wang, S. C. Sun, Y. K. Li, Z. G. Shao and B. L. Yi, *Phys. Chem. Chem. Phys.*, 2013, **15**, 2858–2866.
46 C. Wang, Y. M. Sui, G. J. Xiao, X. Y. Yang, Y. J. Wei, G. T. Zou and B. Zou, *J. Mater. Chem. A*, 2015, **3**, 19669–19673.
47 R. E. Fuentes, H. R. Colón-Mercado and M. J. Martínez-Rodríguez, *J. Electrochem. Soc.*, 2014, **161**, F77–F82.
48 W. Hu, S. L. Chen and Q. H. Xia, *Int. J. Hydrogen Energy*, 2014, **39**, 6967–6976.
49 P. Lettenmeier, J. Majchel, L. Wang, V. A. Saveleva, S. Zafeiratos, E. R. Savinova, J. J. Gallet, F. Bournel, A. S. Gago and K. A. Friedrich, *Chem. Sci.*, 2018, **9**, 3570–3579.
50 G. Q. Li, K. Li, L. Yang, J. F. Chang, R. P. Ma, Z. J. Wu, J. J. Ge, C. P. Liu and W. Xing, *ACS Appl. Mater. Interfaces*, 2018, **10**, 38117–38124.
51 G. Q. Li, S. T. Li, J. J. Ge, C. P. Liu and W. Xing, *J. Mater. Chem. A*, 2017, **5**, 17221–17229.
52 L. Wang, P. Lettenmeier, U. Golla-Schindler, P. Gazdzicki, N. A. Cañas, T. Morawietz, R. Hiesgen, S. S. Hosseiny, A. S. Gago and K. A. Friedrich, *Phys. Chem. Chem. Phys.*, 2016, **18**, 4487–4495.
53 J. Lim, D. Park, S. S. Jeon, C. W. Roh, J. Choi, D. Yoon, M. Park, H. Jung and H. Lee, *Adv. Funct. Mater.*, 2018, **28**, 1704796.
54 V. Pfeifer, T. E. Jones, S. Wrabetz, C. Massué, J. J. Velasco Vélez, R. Arrigo, M. Scherzer, S. Piccinin, M. Hävecker, A. Knop-Gericke and R. Schlögl, *Chem. Sci.*, 2016, **7**, 6791–6795.
55 J. R. Feng, F. Lv, W. Y. Zhang, P. H. Li, K. Wang, C. Yang, B. Wang, Y. Yang, J. H. Zhou, F. Lin, G. C. Wang and S. J. Guo, *Adv. Mater.*, 2017, **29**, 1703798.
56 Q. R. Shi, C. Z. Zhu, H. Zhong, D. Su, N. Li, M. H. Engelhard, H. B. Xia, Q. Zhang, S. Feng, S. P. Beckman, D. Du and Y. H. Lin, *ACS Energy Lett.*, 2018, **3**, 2038–2044.
57 Y. C. Lin, Z. Q. Tian, L. J. Zhang, J. Y. Ma, Z. Jiang, B. J. Deibert, R. X. Ge and L. Chen, *Nat. Commun.*, 2019, **10**, 162.
58 O. Kasian, S. Geiger, T. Li, J. P. Grote, K. Schweinar, S. Y. Zhang, C. Scheu, D. Raabe, S. Cherevko, B. Gault and K. J. J. Mayrhofer, *Energy Environ. Sci.*, 2019, **12**, 3548–3555.
59 S. Geiger, O. Kasian, M. Ledendecker, E. Pizzutilo, A. M. Mingers, W. T. Fu, O. Diaz-Morales, Z. Z. Li, T. Oellers, L. Fruchter, A. Ludwig, K. J. J. Mayrhofer, M. T. M. Koper and S. Cherevko, *Nat. Catal.*, 2018, **1**, 508–515.
60 A. Zagalskaya and V. Alexandrov, *ACS Catal.*, 2020, **10**, 3650–3657.
61 J. Y. Chen, P. X. Cui, G. Q. Zhao, K. Rui, M. M. Lao, Y. P. Chen, X. S. Zheng, Y. Z. Jiang, H. G. Pan, S. X. Dou and W. P. Sun, *Angew. Chem., Int. Ed.*, 2019, **58**, 12540–12544.
62 Y. B. Chen, H. Y. Li, J. X. Wang, Y. H. Du, S. B. Xi, Y. M. Sun, M. Sherburne, J. W. Ager, A. C. Fisher and Z. C. J. Xu, *Nat. Commun.*, 2019, **10**, 572.
63 O. Diaz-Morales, S. Raaijman, R. Kortlever, P. J. Kooyman, T. Wezendonk, J. Gascon, W. T. Fu and M. T. M. Koper, *Nat. Commun.*, 2016, **7**, 12363.